

High-Performance Photothermal Conversion of Narrow-Bandgap Ti_2O_3 Nanoparticles

Juan Wang, Yangyang Li, Lin Deng, Nini Wei, Yakui Weng, Shuai Dong, Dianpeng Qi, Jun Qiu, Xiaodong Chen,* and Tom Wu*

Conversion of solar energy to heat is one of the most important aspects in solar energy harvesting. It enables a broad range of applications including solar power generation, chemical separation/purification, as well as seawater desalination.^[1–4] In conventional solar-to-heat systems, photothermal materials were mainly used as light absorbers to increase the absorption and conversion efficiency of solar energy.^[5–17] For instance, metallic nanoparticles such as gold nanoparticles can produce heat through a surface plasmonic effect, dramatically increasing environment temperatures.^[8] This phenomenon has been utilized in various applications such as solar vapor generation, liquid–liquid phase separation, and localized water heating.^[9–11] Besides, polypyrrole organic polymers^[12–14] and carbon-based composite materials^[15–17] have also presented photon-to-thermal conversion ability due to their strong light absorption. Despite these advancements, the metallic nanomaterials only respond to a limited range of solar spectrum,^[18] and most of light-absorbing organic materials suffer from aging instability.^[19] Therefore, it remains a challenge to develop photothermal converters with high efficiency and stability to be easily scaled up for practical uses.

Generally, ideal photothermal materials must meet the following criteria: i) they must have a wide absorption capability covering the full solar spectrum range (from 250 to 2500 nm); ii) they must be less emissive, which ensures the largest photo-to-heat conversion efficiency; and iii) they must be made from

world abundant elements and can be cost-effectively scaled-up for industrial productions. Titanium is the ninth earth abundant element and its metal oxide composites such as titanium dioxide have been intensively investigated due to the photore-sponse capability, low cost, and high thermal stability.^[20–28] However, owing to the intrinsic large bandgap (≈ 3 eV), typical titanium dioxide only responds to UV irradiation with wavelength < 400 nm. During the past decades, considerable efforts have been made to narrow the bandgap of titanium dioxide to absorb the solar energy in visible spectrum range.^[29–31] The state-of-the-art studies on reduced titanium dioxides have narrowed the bandgap to 1.5 eV, extending the photoresponse of titanium dioxide to the wavelength of 800 nm and around 40% of the total solar energy.^[32–39] However, it is desirable to narrow the bandgap of titanium oxides further to less than 0.5 eV in order to develop efficient full spectrum solar energy converter with high solar energy utilization.

Based on the considerations above, herein we report the first example of using nanosized titanium sesquioxide (Ti_2O_3) as a novel light absorber for solar–thermal conversion. The fairly small bandgap (≈ 0.1 eV) endows Ti_2O_3 with the ability to absorb solar energy in the full spectrum range. More importantly, we find that the light absorption ability of conventional bulk Ti_2O_3 can be improved when the material size is reduced to nanoscale as a result of enhanced light scattering among the nanoparticles.^[8] By combining the ultrasmall bandgap and the nanosized features of Ti_2O_3 nanoparticles, we successfully achieve a nearly 100% internal and $\approx 92\%$ external solar–thermal conversion efficiency outperforming most of the conventional photothermal materials.

In a typical experiment, commercial Ti_2O_3 powders (100 mesh) were used as starting materials and ground to nanoparticles with a ball milling time of 24 h. The powder X-ray diffraction pattern of the post-ground Ti_2O_3 sample can be well indexed to a corundum phase (**Figure 1a**). The corundum Ti_2O_3 has a trigonal structure ($a = b = 5.15$ Å; $c = 13.61$ Å) with an $R\bar{3}c$ space group (**Figure 1b**). A representative scanning electron microscopy (SEM) image of the as-prepared Ti_2O_3 nanoparticles indicates an average diameter of ≈ 400 nm (**Figure 1c**). The high-resolution transmission electron microscopy and the corresponding selected-area electron diffraction patterns reveal excellent single crystallinity of the Ti_2O_3 nanoparticles (**Figure 1d,e**). Notably, the micro-Raman scattering spectra show that there is a Raman peak shift in Ti_2O_3 nanoparticles in comparison to the bulk (**Figure S1**, Supporting Information), which is probably due to the change of surface strain of the Ti_2O_3 particles during the milling process.^[40,41] The energy dispersive spectroscopy (EDS) results indicate the existence

Dr. J. Wang, Dr. D. Qi, Dr. J. Qiu, Prof. X. Chen
School of Materials Science and Engineering
Nanyang Technological University
50 Nanyang Avenue 639798, Singapore
E-mail: chenxd@ntu.edu.sg

Y. Li, Prof. T. Wu
Materials Science and Engineering
King Abdullah University of Science and Technology
Thuwal 23955-6900, Kingdom of Saudi Arabia
E-mail: tao.wu@kaust.edu.sa

Dr. L. Deng
Advanced Membrane and Porous Materials Center
King Abdullah University of Science and Technology
Thuwal 23955-6900, Kingdom of Saudi Arabia

N. Wei
Imaging and Characterization Core lab
King Abdullah University of Science and Technology
Thuwal 23955-6900, Kingdom of Saudi Arabia

Y. Weng, Prof. S. Dong
Department of Physics
Southeast University
Nanjing 211189, China

DOI: 10.1002/adma.201603730



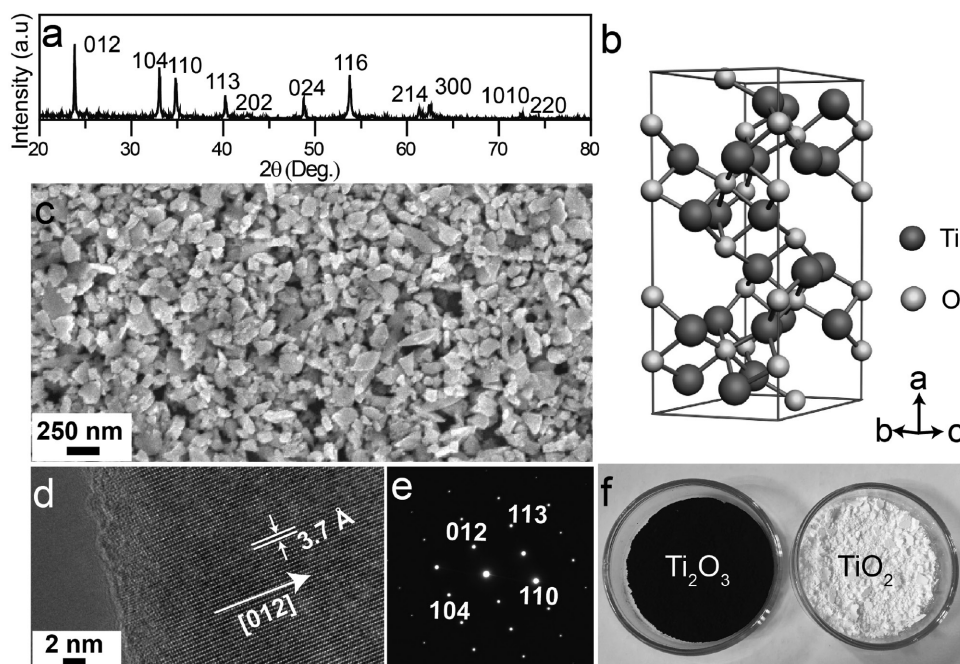


Figure 1. a) X-ray powder diffraction pattern of the as-prepared Ti_2O_3 nanoparticles. b) Schematic representation of the Ti_2O_3 corundum unit cell. c) SEM image of the as-fabricated Ti_2O_3 nanoparticles. d) High-resolution TEM image of a single nanoparticle. e) The corresponding electron diffraction patterns of the Ti_2O_3 nanoparticle. f) Photograph of the as-synthesized Ti_2O_3 nanoparticles (left) and the commercially available TiO_2 powders (right).

of a trace amount of silica in the as-prepared Ti_2O_3 nanoparticles, which was possibly brought by the agate used in the ball milling process (Figure S2, Supporting Information). The chemical stability of the Ti_2O_3 nanocrystals at different temperatures and atmospheres was further investigated. Generally, Ti_2O_3 nanocrystals appear in black and are stable under normal outdoor conditions (Figure 1f). Under air atmosphere, the Ti_2O_3 nanocrystals are stable at temperatures up to 400 °C. The nanocrystals transfer from corundum Ti_2O_3 to rutile TiO_2 at temperature above 500 °C. However, under the argon atmosphere, the Ti_2O_3 nanocrystals remain in the corundum phase when heated to 1000 °C (Figure S3, Supporting Information).

Density functional theory calculations were further carried out to understand the band features of the Ti_2O_3 nanoparticles based on the Heyd–Scuseria–Ernzerhof (HSE) exchange calculation method.^[42,43] As shown by the projected and total electronic density of states (PDOS/DOS), the bandgap of Ti_2O_3 was calculated to be as small as 0.09 eV, which is in line with the previous reports.^[44–46] The electronic states around the Fermi energy are mainly contributed by Ti 3d orbitals (Figure 2a). The high population of Ti 3d orbitals between -2 and 2 eV enables broad band absorption of Ti_2O_3 from the band edge (0.09 eV) to >4 eV (<310 nm), hereby, the ability of absorbing the full spectrum solar energy. It should be pointed out that the overwhelming majority of photons from solar emission has significantly higher energy than the bandgap of Ti_2O_3 , which leads to the generation of above-bandgap electron–hole pairs in Ti_2O_3 under sunlight irradiation. The above-bandgap electrons and holes then relax to the band edges and convert the extra energy into heat through a thermalization process (Figure 2b).^[47] Note that the relaxation dynamics of the above-bandgap electrons

and holes could be quite complicated, but it may be dominated by an acoustic-phonon scattering mechanism.^[47] This is in stark contrast with conventional wide-bandgap semiconductors in which most of the light energy absorbed reemits as photons after recombination of electron–hole pairs near the bandgap edge (Figure 2b). Under a standard Air Mass 1.5 sunlight with an average photon energy of ≈ 1.6 eV, the direct thermalization in Ti_2O_3 nanoparticles may consume over 94% (≈ 1.51 eV) of the photon energy upon absorption. Meanwhile, the rest of the band edge energy may also contribute to the heat generation as it is already located in the infrared range and can be thermally absorbed through the vibration of crystal lattice. The ultranarrow bandgap of Ti_2O_3 implies that it may be a promising material for applications in highly efficient solar–thermal conversion.

To experimentally assess the absorption capacity, we further measured the diffuse reflectance of Ti_2O_3 nanoparticles. As presented in Figure 2c, the Ti_2O_3 nanoparticles show excellent absorption features over the whole range of the solar spectrum with an average reflectance of less than 10%. This is in contrast with TiO_2 which only absorbs light in the UV region, or graphite with an average reflectance of around 20%. In addition, the commercial Ti_2O_3 powders present the similar reflectance feature with the Ti_2O_3 nanoparticles but a lower absorption capability. This is mainly due to the less efficient surface light scattering for bulk materials. Furthermore, we found that Ti_2O_3 nanoparticles (≈ 400 nm) have the ability to absorb almost 94% of UV, 95% of visible, and 89% of infrared solar irradiation with a total absorption capacity of 92.5% over the whole solar spectrum (Table 1). It should be pointed out that the absorption efficiency of Ti_2O_3 nanoparticles can be improved by further

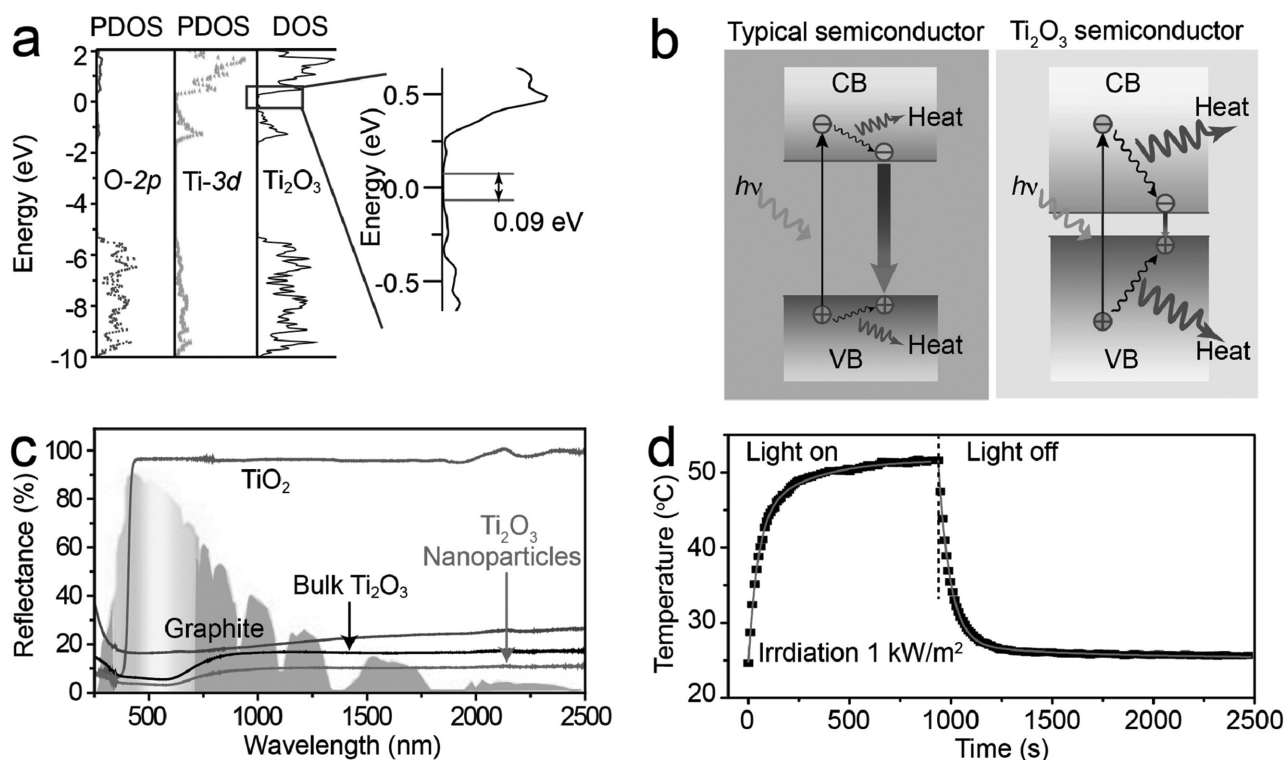


Figure 2. a) PDOS/DOS of Ti₂O₃ nanoparticles derived from first-principles calculations. b) Illustration of the electron–hole generation and relaxation in a normal semiconductor (left) and in narrow-bandgap Ti₂O₃ (right). c) Diffuse reflectance spectra of commercial TiO₂, graphite, commercial Ti₂O₃ powder, and Ti₂O₃ nanoparticles. The inserted background is a solar irradiation spectrum. d) A typical temperature–time relationship showing the increase in the temperature of the Ti₂O₃ sample under irradiation from a solar simulator and the decay trace of temperature after the irradiation is turned off.

reducing the particle size. As an evidence of the size effect, we found that the overall absorption was enhanced by around 1% when the average size of the Ti₂O₃ nanoparticles was reduced from ≈400 to ≈350 nm (Figure S6, Supporting Information). Further reduction of the nanoparticle size might improve the light absorption, which however will require other synthesis routes other than the ball milling process. Notably, the absorption ability of Ti₂O₃ nanoparticles is much higher than conventional photosensitive titanium oxides, and it is even better than some carbon-based materials such as graphite.

With such high absorption capability, the Ti₂O₃ nanoparticles are promising to produce high photothermal efficiency as

Table 1. Solar absorption of photothermal materials in different spectrum region.

Sample	Total	UV ^{a)}	Visible ^{b)}	Infrared ^{c)}	References
Solar	100%	7%	50%	43%	[54]
Black TiO ₂	30–83%	5–6%	24–39%	1–38%	[32,35]
Pristine TiO ₂	5%	5%	–	–	[35]
Graphite	80.5%	5.7%	40.6%	34.2%	This work
Commercial Ti ₂ O ₃	85.4%	6.4%	42.6%	36.4%	This work
Ti ₂ O ₃ nanoparticles	92.5%	6.6%	47.4%	38.5%	This work

^{a)}UV light: <400 nm; ^{b)}visible light: 400–760 nm; ^{c)}infrared light: >760 nm.

anticipated above. The external photothermal conversion efficiency η_{ext} is defined by the ratio of the generated heat Q versus the irradiation energy of photon flux q :

$$\eta_{\text{ext}} = \frac{Q}{q} \quad (1)$$

We applied a modified photocalorimetric method to determine Q for Ti₂O₃ samples at an irradiation photon flux of 1 kW m⁻² produced by a solar simulator.^[48] Under solar light irradiation, a material would be heated up from room temperature T_{surr} to a maximum temperature T_{max} at which the heat Q generated by the material equals the heat Q_{surr} dissipated to the surrounding:

$$Q = Q_{\text{surr}} = h \times s \times (T_{\text{max}} - T_{\text{surr}}) \quad (2)$$

where h refers to the heat transfer coefficient, and s is the surface area of the material for heat dissipation. By investigating four individual compressed round pill samples of Ti₂O₃, we determined the $T_{\text{max}} - T_{\text{surr}}$ of the Ti₂O₃ samples to be ≈24.5 °C (Figure 2d). The value of hs was found to be ≈3.8 mW °C⁻¹ by fitting the temperature cooling stages of the samples with an exponential decay function (see the Supplementary Information for details). The external solar–heat conversion efficiency η_{ext} was calculated to be 92.1 ± 3.2% according to Equation (1) and (2). It is worth mentioning that ≈92% of the total solar

energy was absorbed according to the diffuse reflectance measurements (Table 1). It indicates that the Ti_2O_3 nanoparticles have converted almost all of the absorbed photons to heat with internal conversion efficiency close to 100%.

The outstanding light absorption property of Ti_2O_3 nanoparticles offers unique opportunities for the development of highly efficient solar–thermal conversion systems. As a proof of concept, we demonstrate the use of Ti_2O_3 nanoparticles for solar-enabled water evaporation. In our design, a thin layer of Ti_2O_3 nanoparticles was supported by a cellulose membrane to form a double-layer-structured device (Figure S4 and S5, Supporting Information). The thin-film device is then floated on water surface and acted as a localized photothermal converter. Under solar radiation, the Ti_2O_3 can efficiently heat up the surface portion of water, generating steam from the water surface (Figure 3a). By collecting the condensed water from the steam, it is possible to use this design for desalination and water purification using sunlight as the only power source.^[11,16]

In a typical experiment, Ti_2O_3 nanoparticles were first dispersed in water, followed by deposition on a cellulose membrane under vacuum condition (Figure 3b). Cellulose membrane was chosen as a bottom supporting layer because of its unique inner microporous structure and hydrophilicity (Figure 3c). The microporous structure of the cellulose membrane enables efficient absorption of water through capillary effect. This effect enables more rapid replenishment of surface water after evaporation, while the hydrophilicity would benefit

the water adhesion and speed up the water transfer upward. As an added benefit, cellulose membrane can minimize deleterious heat loss from Ti_2O_3 layers to bulk water due to its relatively low thermal conductivity ($0.02 \text{ W m}^{-1} \text{ K}^{-1}$).^[49] Under illumination of a solar simulator at power density of 7 kW m^{-2} , the solar–thermal system can be quickly heated up in 2 min and generates visible steam flow on top of the water surface (Figure 3d and Figure S5, Supporting Information). Notably, when the temperature of the film surface reached $70 \text{ }^\circ\text{C}$, the temperature at most of the other parts remains almost unchanged (Figure 3e). This is due to a strong localized solar light heating effect induced by the Ti_2O_3 nanoparticles.

It should be mentioned that the localized heat effect can significantly improve the solar vapor generation by preventing energy loss during heating of the bulk water.^[11,16] Without the Ti_2O_3 thin-film device, we found that the temperature increment of bulk water was almost negligible after 15 min continuous solar light irradiation at 5 kW m^{-2} (Figure 4a). By contrast, under the identical illumination condition, the surface temperature of seawater sample with Ti_2O_3 thin-film device was heated to about $50 \text{ }^\circ\text{C}$ (Figure 4b). Quantitative measurements on the temperature variations further prove that the localized heating is originated from the concentration of solar energy by the Ti_2O_3 layer rather than the block of direct radiation by a cellulose layer. As shown in Figure 4c and Figure S7 (Supporting Information), Ti_2O_3 thin-film device induced a much faster temperature increase for water on the top surface than that at the bottom. The temperature difference between the top and bottom areas continuously increased and reached $\approx 23 \text{ }^\circ\text{C}$ after 15 min of irradiation. By contrast, the temperature difference in a control experiment without the Ti_2O_3 thin-film device was less than $0.5 \text{ }^\circ\text{C}$, indicating the absence of localized heating. We further investigated the performance of solar vapor generation of Ti_2O_3 by monitoring the weight loss of seawater during evaporation. As expected, Ti_2O_3 induced enhanced evaporation efficiency under various irradiation powers. We observed evaporation rates of $1.32 \text{ kg m}^{-2} \text{ h}^{-1}$ and $5.03 \text{ kg m}^{-2} \text{ h}^{-1}$ for Ti_2O_3 samples at 1 and 5 kW m^{-2} solar irradiance, which are 2.65 and 4.18 times higher than pure water evaporation (Figure 4d,e). The Ti_2O_3 nanoparticle-based thin-film device also presents higher solar vapor generation rate than graphite and commercial Ti_2O_3 powders (Figure S8 and S9, Supporting Information). The durability of the Ti_2O_3 thin film was also investigated under different light illumination intensities. The film presented stable performances during 25 experiment cycles, indicating good recycle stability. Taken together, these results unambiguously indicate the feasibility of using the Ti_2O_3 nanoparticles for efficient solar vapor generation.

In conclusion, we have demonstrated for the first time the possibility of using Ti_2O_3 nanoparticles as an efficient photothermal material taking advantage of both its narrow bandgap and nanoscale-sized features. The narrow-bandgap structure enables Ti_2O_3 nanoparticles to absorb the full solar spectrum, while the nanoscale-sized feature further enhances the absorption efficiency. Furthermore, we fabricated a Ti_2O_3 nanoparticle-based thin-film device and validated its high solar vapor generation efficiency and stability, indicating its potential use in seawater desalination and purification. Considering the increasing demand of clean and recycle solar energy usage,

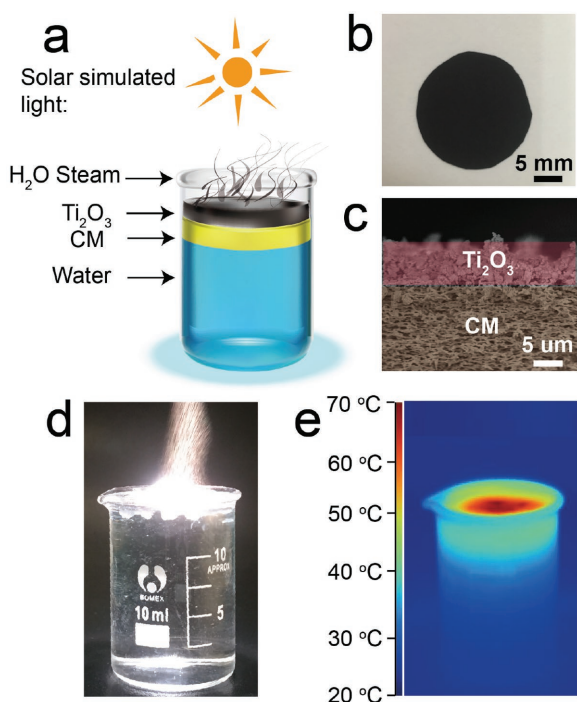


Figure 3. a) A schematic diagram of the solar water steam evaporation design where the cellulose membrane (CM) was used to load the Ti_2O_3 nanoparticle. b) Photograph of the double-layer film. c) SEM cross-section image of the double layered film structure. d) Photograph of the water steam generated under solar illumination of 7 kW m^{-2} , with the Ti_2O_3 nanoparticle-based thin film floating on top of the water. e) Corresponding IR photograph of (d) taken by an IR camera.

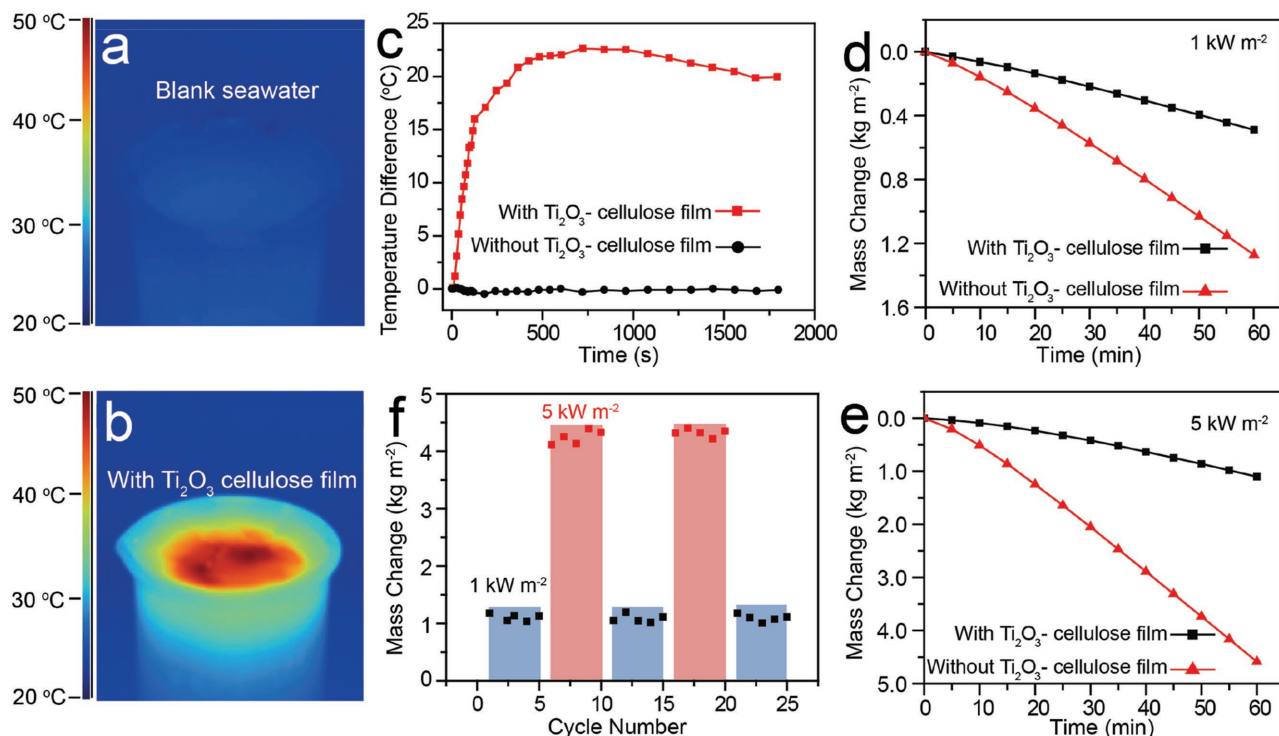


Figure 4. a,b) IR photographs of 10 mL beakers with seawater inside (a) and Ti₂O₃ nanoparticle-based thin film on top of the water surface (b), respectively. The light illumination intensity is 5 kW m⁻². c) Temperature difference between the top water surface and the bottom section in the beaker upon solar light irradiation. The red curve presents the data taken on the seawater with Ti₂O₃ thin film, while the black curve presents the seawater sample without the film. The light illumination intensity is 5 kW m⁻². d,e) Evaporation water weights against time with and without Ti₂O₃ thin-film device under the solar illumination, under 1 kW m⁻² (d) and 5 kW m⁻² (e). f) Evaporation cycle performance of the Ti₂O₃-based thin film under different solar simulation light intensities. Each cycle was sustained for 1 h. All experiments were conducted at ambient temperature of 20 °C and humidity of 55%.

our findings provide a promising material not only for solar-thermal energy conversion but also for a wider range of applications such as photothermal therapy and thermal catalysis.

Experimental Section

Reagents: Commercial Ti₂O₃ powders (100 mesh), TiO₂ (<5 μm), and graphite (<2 μm) were purchased from Sigma–Aldrich. Cellulose membrane was purchased from Merck Millipore Company. All the materials were used as starting materials without further purification. The sea water was taken from the Palawan beach in the Sentosa Island, Singapore.

Fabrication of the Ti₂O₃ Nanoparticles: Ti₂O₃ nanoparticles were obtained by the ball milling technique. Agate balls (Diameter: 10 mm and 5 mm) and agate containers were applied in the ball milling process. The milling speed was fixed at 300 rpm, and the milling process took 24 and 48 h to produce different Ti₂O₃ nanoparticle sizes.

Fabrication of the Ti₂O₃-Nanoparticle-Based Film Device: 10 mg of Ti₂O₃ nanoparticles (average diameter: 400 nm) was dispersed well in 10 mL deionized (DI) water, under the assistance of ultrasonic bath. The dispersed mixture was deposited on the cellulose membrane under vacuum. The performed film was placed on a heat plate and the temperature was kept at 60 °C for 10 min. After cooling down, the film was stored in a Petri dish for further use. The fabrication of graphite and bulk Ti₂O₃ powder-based thin films followed the same procedure except that Ti₂O₃ nanoparticles were replaced with graphite or bulk Ti₂O₃ powders.

Characterization: The SEM image was implemented by the field emission scanning electron microscopy (FESEM, JEOL JSM-6340F).

The crystallographic phases of the sample were determined by Bruker D8 ADVANCE diffractometer, equipped with the Cu K_α radiation source and LynxEye detector. Raman measurements were carried out with a confocal micro-Raman system (Horiba Aramis/Jobin Yvon HR800) at ambient conditions, using a solid state laser (excitation wavelength is 473 nm). Duoscan mode was used to collect the Raman data from the Ti₂O₃ nanoparticles, in order to decrease the energy focused on the nanoparticles. The TEM image, electron diffraction pattern, and EDS spectrum were collected by a FEI Titan commercial TEM, operated at 300 kV. The reflectance measurements were performed via Cary 5000 UV–Vis NIR Spectrophotometer. All IR photographs were taken via a Fluke Ti300 Infrared Camera.

First-Principles Calculations: The electronic calculations were performed based on the projector augmented wave approach as implemented in the Vienna ab initio simulation package.^[50–52] Using the Dudarev implementation,^[53] the Hubbard U_{eff} ($=U - J$) was imposed on Ti 3d orbitals. First, the internal atomic positions were optimized with GGA+ U . Then the electronic structures were studied by using the hybrid function based on the HSE exchange. In the HSE calculation, the structural optimization of electronic self-consistent interactions was performed using a plane-wave cut-off energy of 450 eV, and a Γ -centered Monkhorst–Pack k -point mesh of $5 \times 5 \times 5$. The bandgap of 0.09 eV was obtained when $U_{\text{eff}} = 0$ eV.

Supporting Information

Supporting Information is available from the Wiley Online Library or from the author.

Acknowledgements

J.W. and Y.L. contributed equally to this work. This work was supported in part by National Research Foundation, Prime Minister's Office, Singapore under its Campus for Research Excellence and Technological Enterprise (CREATE) Programme of Nanomaterials for Energy and Water management. Y.L. and T.W. acknowledge funding support from the King Abdullah University of Science and Technology (KAUST).

Received: July 14, 2016

Revised: August 26, 2016

Published online: November 11, 2016

- [1] N. S. Lewis, *Science* **2016**, 351, 353.
- [2] Y. Parent, D. Blake, K. Magrini-Bair, C. Lyons, C. Turchi, A. Watt, E. Wolfrum, M. Prairie, *Sol. Energy* **1996**, 56, 429.
- [3] H. Tong, S. X. Ouyang, Y. P. Bi, N. Umezawa, M. Oshikiri, J. H. Ye, *Adv. Mater.* **2012**, 24, 229.
- [4] D. Bahnemann, *Sol. Energy* **2004**, 77, 445.
- [5] D. Kraemer, B. Poudel, H. P. Feng, J. C. Caylor, B. Yu, X. Yan, Y. Ma, X. W. Wang, D. Wang, A. Muto, K. McEnaney, M. Chiesa, Z. Ren, G. Chen, *Nat. Mater.* **2011**, 10, 532.
- [6] G. M. Ayoub, A. A. Hindi, L. Malaeb, *Desalination* **2009**, 242, 128.
- [7] Y. Zeng, J. F. Yao, B. A. Horri, K. Wang, Y. Z. Wu, D. Li, H. T. Wang, *Energy Environ. Sci.* **2011**, 4, 4074.
- [8] O. Neumann, A. S. Urban, J. Day, S. Lal, P. Nordlander, N. J. Halas, *ACS Nano* **2013**, 7, 42.
- [9] O. Neumann, A. D. Neumann, E. Silva, C. Ayala-Orozco, S. Tian, P. Nordlander, N. J. Halas, *Nano Lett.* **2015**, 15, 7880.
- [10] P. Tao, W. Shang, C. Y. Song, Q. C. Shen, F. Y. Zhang, Z. Luo, N. Yi, D. Zhang, T. Deng, *Adv. Mater.* **2015**, 27, 428.
- [11] Y. M. Liu, S. T. Yu, R. Feng, A. Bernard, Y. Liu, Y. Zhang, H. Z. Duan, W. Shang, P. Tao, C. Y. Song, T. Deng, *Adv. Mater.* **2015**, 27, 2768.
- [12] L. B. Zhang, B. Tang, J. B. Wu, R. Y. Li, P. Wang, *Adv. Mater.* **2015**, 27, 4889.
- [13] Y. Liu, D. D. Wang, L. Zhao, M. Lin, H. Z. Sun, H. C. Sun, B. Yang, *RSC Adv.* **2016**, 6, 15854.
- [14] T. Park, J. Na, B. Kim, Y. Kim, H. Shin, E. Kim, *ACS Nano* **2015**, 9, 11830.
- [15] Y. Ito, Y. Tanabe, J. H. Han, T. Fujita, K. Tanigaki, M. W. Chen, *Adv. Mater.* **2015**, 27, 4302.
- [16] H. Ghasemi, G. Ni, A. M. Marconnet, J. Loomis, S. Yerci, N. Miljkovic, G. Chen, *Nat. Commun.* **2014**, 5, 4449.
- [17] G. Katumba, L. Olumkor, A. Forbes, G. Makiwa, B. Mwakikunga, J. Lu, E. Wäcklgård, *Sol. Energy Mater. Sol. Cells* **2008**, 92, 1285.
- [18] S. J. Norton, T. Vo-Dinh, *J. Appl. Phys.* **2016**, 119, 083105.
- [19] V. T. Truong, *Synth. Met.* **1992**, 52, 33.
- [20] X. J. Lang, J. C. Zhao, X. D. Chen, *Angew. Chem., Int. Ed.* **2016**, 55, 4697.
- [21] L. T. Su, S. K. Karuturi, J. S. Luo, L. J. Liu, X. F. Liu, J. Guo, T. C. Sum, R. R. Deng, H. J. Fan, X. G. Liu, A. J. Y. Tok, *Adv. Mater.* **2013**, 25, 1603.
- [22] Y. Y. Zhang, B. Wu, Y. X. Tang, D. P. Qi, N. Wang, X. T. Wang, X. L. Ma, T. C. Sum, X. D. Chen, *Small* **2016**, 12, 2291.
- [23] D. V. Bavykin, J. M. Friedrich, F. C. Walsh, *Adv. Mater.* **2006**, 18, 2807.
- [24] X. B. Chen, S. S. Mao, *Chem. Rev.* **2007**, 107, 2891.
- [25] Z. H. Zhao, J. Tian, Y. H. Sang, A. Cabot, H. Liu, *Adv. Mater.* **2015**, 27, 2557.
- [26] B. L. Ellis, P. Knauth, T. Djenizian, *Adv. Mater.* **2014**, 26, 3368.
- [27] R. B. Jiang, B. X. Li, C. H. Fang, J. F. Wang, *Adv. Mater.* **2014**, 26, 5274.
- [28] A. Frölich, J. Fischer, T. Zebrowski, K. Busch, M. Wegener, *Adv. Mater.* **2013**, 25, 3588.
- [29] S. U. M. Khan, M. Al-shahry, W. B. Ingler Jr., *Science* **2002**, 297, 2243.
- [30] R. Asahi, T. Morikawa, T. Ohwaki, K. Aoki, Y. Taga, *Science* **2001**, 293, 269.
- [31] G. Ou, Z. W. Li, L. Cheng, Z. Liu, H. Wu, *Nano Res.* **2016**, 9, 1236.
- [32] X. B. Chen, L. Liu, P. Y. Yu, S. S. Mao, *Science* **2011**, 331, 746.
- [33] W. Zhou, W. Li, J. Q. Wang, Y. Qu, Y. Yang, Y. Xie, K. F. Zhang, L. Wang, H. G. Fu, D. Y. Zhao, *J. Am. Chem. Soc.* **2014**, 136, 9280.
- [34] H. Y. Zhang, Y. F. Zhao, S. Chen, B. Yu, J. L. Xu, H. J. Xu, L. D. Hao, Z. M. Liu, *J. Mater. Chem. A* **2013**, 1, 6138.
- [35] Z. Wang, C. Y. Yang, T. Q. Lin, H. Yin, P. Chen, D. Y. Wan, F. F. Xu, F. Q. Huang, J. H. Lin, X. M. Xie, M. H. Jiang, *Adv. Funct. Mater.* **2013**, 23, 5444.
- [36] S. Tominaka, Y. Tsujimoto, Y. Matsushita, K. Yamaura, *Angew. Chem., Int. Ed.* **2011**, 50, 7418.
- [37] N. Liu, C. Schneider, D. Freitag, M. Hartmann, U. Venkatesan, J. Muller, E. Spiecker, P. Schmuki, *Nano Lett.* **2014**, 14, 3309.
- [38] X. B. Chen, L. Liu, F. Q. Huang, *Chem. Soc. Rev.* **2015**, 44, 1861.
- [39] J. J. Xu, G. L. Zhu, T. Q. Lin, Z. L. Hong, J. Wang, F. Q. Huang, *RSC Adv.* **2015**, 5, 85928.
- [40] V. Swamy, B. C. Muddle, Q. Dai, *Appl. Phys. Lett.* **2006**, 89, 163118.
- [41] J. E. Spanier, R. D. Robinson, F. Zhang, S. W. Chan, I. P. Herman, *Phys. Rev. B* **2001**, 64, 245407.
- [42] J. Heyd, G. E. Scuseria, M. Ernzerhof, *J. Chem. Phys.* **2003**, 118, 8207.
- [43] J. Heyd, G. E. Scuseria, M. Ernzerhof, *J. Chem. Phys.* **2006**, 124, 219906.
- [44] H. Nakatsugawa, E. Iguchi, *Phys. Rev. B* **1997**, 56, 12931.
- [45] A. I. Poteryaev, A. I. Lichtenstein, G. Kotliar, *Phys. Rev. Lett.* **2004**, 93, 086401.
- [46] V. Singh, J. J. Pulikkotil, *J. Alloys Compd.* **2016**, 658, 430.
- [47] M. Umlauff, J. Hoffmann, H. Kalt, W. W. Langbein, J. M. Hvam, M. Scholl, J. Söllner, M. Heuken, B. Jobst, D. Hommel, *Phys. Rev. B* **1998**, 57, 1390.
- [48] D. K. Roper, W. Ahn, M. Hoepfner, *J. Phys. Chem. C* **2007**, 111, 3636.
- [49] A. Alkudhiri, N. Darwish, N. Hilal, *Desalination* **2012**, 287, 2.
- [50] G. Kresse, J. Hafner, *Phys. Rev. B* **1993**, 47, 558.
- [51] G. Kresse, J. Furthmüller, *Phys. Rev. B* **1996**, 54, 11169.
- [52] P. E. Blochl, *Phys. Rev. B* **1994**, 50, 17953.
- [53] S. L. Dudarev, A. P. Sutton, *Phys. Rev. B* **1998**, 57, 1505.
- [54] C. A. Gueymard, *Sol. Energy* **2004**, 76, 423.